ACS APPLIED MATERIALS & INTERFACES

Research Article

www.acsami.org

Unprecedented Activity of Bifunctional Electrocatalyst for High Power Density Aqueous Zinc–Air Batteries

Mengfan Wang, Tao Qian,* Sisi Liu, Jinqiu Zhou, and Chenglin Yan*

Soochow Institute for Energy and Materials InnovationS, College of Physics, Optoelectronics and Energy & Collaborative Innovation Center of Suzhou Nano Science and Technology, Soochow University, Suzhou 215006, China

Key Laboratory of Advanced Carbon Materials and Wearable Energy Technologies of Jiangsu Province, Soochow University, Suzhou 215006, China

Supporting Information

ABSTRACT: The development of nonprecious metal catalysts with desirable bifunctional activities to supersede noble metal catalysts is of vital importance for high performance aqueous zinc–air batteries. Here, an unprecedented activity of bifunctional electrocatalyst is reported by in situ growth of nitrogen-enriched carbon nanotubes with transition metal composite. The resultant catalyst delivers surprisingly high OER (potential@10 mA cm^{-2} of 1.58 V) and ORR (onset potential of 0.97 V, half-wave potential of 0.86 V) performance. The overall oxygen electrode activity (overvoltage between ORR and OER) of the catalyst is as low as 0.72 V. In aqueous Zn–air battery tests, primary batteries demonstrate high maximum power density and two-electrode rechargeable batteries also exhibit good cycle performance. The unprecedented electrocatalyst opens up new avenues for developing highly active nitrogen-doped carbon nanotube-supported electrocatalysts and offers prospects for the next generation of fuel cells, metal–air batteries, and photocatalysis applications.

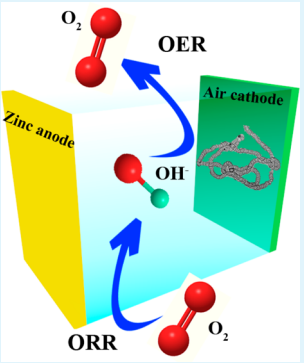

KEYWORDS: *carbon nanomaterial, nitrogen-doping, oxygen reduction reaction, oxygen evolution reaction, non-noble metal catalysts, zinc–air battery*

INTRODUCTION

Global energy crisis drew great concerns among scientists and led them to explore new approaches to reduce greenhouse gas emissions and change the dominance of fossil fuels.[1] Of the options available, renewable energy storage and conversion techniques, such as fuel cells,[2,3] metal–air batteries,[4,5] and water splitting[6,7] were considered efficient and clean solutions to address these problems. The practical applications of these electrochemical systems depended on low-cost but high-active bifunctional electrocatalysts for OER[8] and ORR.[9] Because of the inherently sluggish kinetics of oxygen reactions, lots of catalysts derived from noble metals and their alloys[10−13] were found to give the excellent catalytic performance. In terms of large-scale commercialization, however, these electrocatalysts still did not reach the desire because of their prohibitive cost, scarcity, poor stability, and severe polarization. Furthermore, the single precious metal cannot simultaneously provide sufficient activity for both ORR and OER. In this context, it was highly desirable to develop alternative catalysts with rich resource, low cost, and comparable electrocatalytic activity as substitutions for noble metal-based electrocatalysts.

To meet the above challenges, advanced carbon materials, such as carbon nanotubes,[14,15] (CNTs), carbon nanofibers[16] (CNFs), microporous carbon sheets,[17] graphene,[18−20] and onion-like carbon[21] were extensively studied and considered to be able to replace precious metals because of their superior structural stability, excellent electronic conductivity, and corrosion resistance. Moreover, their catalytic activity can be further improved by introducing heteroatoms, such as N, S, B, and so on.[22−25] In particular, nitrogen offered significant promise as a nonmetal dopant because it can be doped into several locations within the carbon structure, thereby leading to multiple possible configurations and more desirable performance because of the considerable segment of catalytic sites, strong adaptability to the environment, and excellent durability.[26,27] Since N is more electronegative than C, it could make neighboring C atoms electron deficient, thus promoting O_2 adsorption on the carbon nanostructure.[28] Given these considerations, N-doped carbon nanotube (denoted as NCNT) exhibited the one-step process for oxygen reaction with almost doubled diffusion current density compared with nitrogen-free CNT electrode. Except for being prepared from N–C formulations,[29,30] NCNT can also be obtained from transition metal-derived M–N–C (M = Fe or Co).[14,31,32] the existence of the transition metal cation could coordinate with pyridinic N and embed itself into the carbon plane as a possible active site configuration, which provided improved catalytic performance compared with nitrogen-doped carbon. However, the synthesis of such catalysts can be very complicated and low-yield. Therefore, several methods were invented to simplify this

Received: February 16, 2017
Accepted: June 5, 2017
Published: June 5, 2017

DOI: 10.1021/acsami.7b02346
ACS Appl. Mater. Interfaces 2017, 9, 21216−21224

approach.[33] However, NCNTs were just known to be an effective electrocatalyst for ORR, whose activity originated from its local defects that mediated the electronic structure and its surface morphology that regulated atomic arrangement and coordination. To date, there were very limited reports on the use of CNTs or NCNTs as the catalyst for OER. Moreover, CNTs or NCNTs were applied as the support for the catalytically active species rather than a catalyst itself.[34,35]

Many efforts were, therefore, devoted to non-noble-metal oxides. However, recently reported studies indicated that pure metal oxides exhibited undesirable catalytic performance because of self-passivity and low electrical conductivity, thus decreasing active sites and hindering charge transports.[19,34] Most undesirable OER process occurred because the catalysts held the majority of the charge carriers at a high anodic potential and failed to retain enough oxidized species.[36] In this context, cobalt-based metal oxides, such as $MnCoFeO_4$,[37] $Co_xMn_{1-x}O$,[38] and $CoFe_2O_4$,[39] were widely investigated as OER catalysts because of their large exposure extent of active sites and superior electronic conductivity. During the catalytic reactions, however, these metal oxides were easy to aggregate because of large surface energy, which can result in the decrease of the active sites and slow down the transportation of electrons during the oxidation process.[34] By comparison, carbon materials were known to have high surface area, flexible structure and strong adaptability to alkaline environments so that to be desirable to bear advanced mixed metal oxides catalysts. Therefore, N-doped carbon materials coordinating with mixed metal oxides can be excellent catalysts for OER.[34,38]

By integrating the merits, a novel bifunctional electrocatalyst was developed through a synthetic method that enabled a controllable nanoscale synthesis of nitrogen-enriched carbon nanotube encapsuling iron carbide and cobalt−iron-based mixed metal oxide composite (denoted as $Fe_3C/Co(Fe)O_x$@NCNT) by annealing a mixture of polypyrrole-iron (PPy-Fe) coordination complex precursors and Co−Zn additive. As expected, the volatilization of Zn resulted in high surface area with more nitrogen-doping, thus promoting oxygen adsorpotion and facilitating oxygen reactions. Moreover, the resultant $Fe-N_x$ moieties and N-functionalized groups can improve ORR activity, while the combination of $Co(Fe)O_x$ and NCNT with high electric conductivity and stable structure was beneficial to OER activity. The synergistic effect of all above characters finally led to a desirable bifunctional electrocatalyst for oxygen reactions. The resultant $Fe_3C/Co(Fe)O_x$@NCNT delivered surprisingly high OER (potential@10 mA cm^{-2} of 1.58 V), ORR (onset potential of 0.97 V, half-wave potential of 0.86 V) performance, and superior stability in alkaline solution. The overall oxygen electrode activity (overvoltage between ORR and OER) of the $Fe_3C/Co(Fe)O_x$@NCNT was as low as 0.72 V, which was almost the best data among non-noble metal bifunctional electrocatalysts. Noteworthy, $Fe_3C/Co(Fe)O_x$@NCNT was also tested as a real rechargeable Zn−air battery and exhibited good cycle performance and low charging/discharging voltage gap. The resulting sample $Fe_3C/Co(Fe)O_x$@NCNT performed much better than Pt/C or IrO_2, thus providing a new protocol to construct novel low-cost but high-active bifunctional electrocatalysts to be applied in the next generation of energy systems.

RESULTS AND DISCUSSION

The fabrication of $Fe_3C/Co(Fe)O_x$@NCNT followed the general synthetic strategy. In a typical procedure, the precursor, PPy−Fe was prepared[40,41] and Co−Zn composite was synthesized in the methanol solution containing dispersed PPy−Fe coordination complex, followed by a simple thermal treatment at 900 °C with argon gas protection. After washing twice with deionized water, the target products were obtained. During the carbonization process, Co−Zn/PPy−Fe complex gradually degraded to form bamboo-like N-doped carbon nanotubes with Co−Zn encapsulated in it. At the same time, Fe element of PPy−Fe coordination complex was first transformed into Fe_3C and coated on the nanoparticle surface. Zn^{2+} of Co−Zn gradually volatilized while Co and partial Fe were oxidized generating $Fe_3C/Co(Fe)O_x$ nanoparticles within NCNT. The Fe, Co and Zn content of the material as analyzed by ICP were 4.67%, 1.74%, 0.05%, respectively, which were in good agreement with the ideal product. The embedded $Co/Fe-N_x$ moieties and N species in the carbon framework played critical roles in enhancing ORR performance[32,42] while CoO_x and CNT sped up the electron transportation among $Fe_3C/Co(Fe)O_x$ nanoparticles, thus facilitating both ORR and OER processes.

Importantly, the formation of different nanostructures (e.g., lamellar nitrogen-doped carbon (denoted as LNC), spindle/lamella hybrid nitrogen-doped carbon (denoted as SNC/LNC) and carbon nanotube) can be controlled during the preparation process by optimizing the introduction of transition metals into precursors. The morphologies of different samples were clearly depicted under transmission electron microscopy (TEM). As shown in Figure S1a and b, it was found that, without additive, purely carbonized PPy−Fe only presented the lamellar morphology without CNT present, and resultant Fe_3C/FeO_x@lamellar nitrogen-doped carbon (denoted as Fe_3C/FeO_x@LNC). With addition of Zn species in the precursor, the resultant material began to grow spindlelike carbon on the lamellar carbon, which can be considered as a transition state of the growth of nanotubes, with Fe_3C/FeO_x nanoparticles distributing in the SNC/LNC hybrid (denoted as Fe_3C/FeO_x@SNC/LNC, Figure S1c and d). After partially substituting Zn with Co, the end product successfully grew into nanotubes and finally, $Fe_3C/Co(Fe)O_x$@NCNT was obtained as shown in Figure S1e−f and Figure 1a. NCNTs with a diameter of about 20 nm were observed while $Fe_3C/Co(Fe)O_x$ nanoparticles were distributed inside the NCNTs. The high-resolution TEM was shown in Figure 1b, in which all the main characteristics of $Fe_3C/Co(Fe)O_x$@NCNT can be

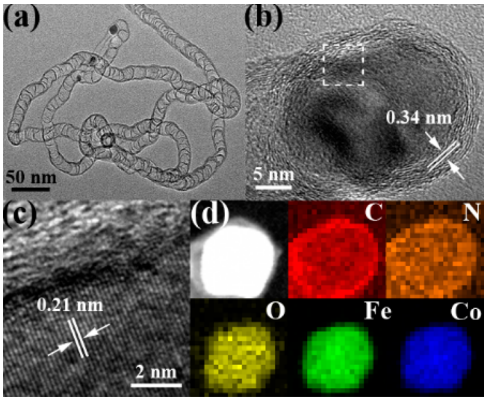

Figure 1. (a) TEM image, (b) high-resolution TEM image, (c) enlarged high-resolution TEM image, and (d) mapping images of $Fe_3C/Co(Fe)O_x$@NCNT.

DOI: 10.1021/acsami.7b02346
ACS Appl. Mater. Interfaces 2017, 9, 21216−21224

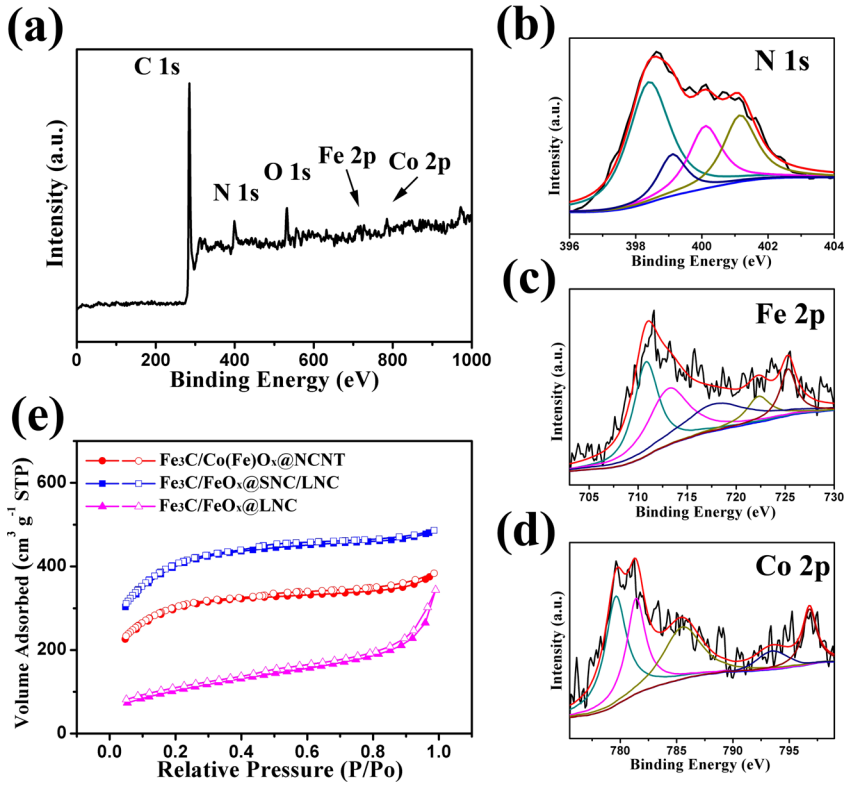

Figure 2. (a) Long-range XPS spectrum, (b) N 1s XPS spectrum, (c) Fe 2p XPS spectrum, and (d) Co 2p XPS spectrum of $Fe_3C/Co(Fe)O_x$@NCNT. (e) N_2 sorption isotherms for $Fe_3C/Co(Fe)O_x$@NCNT, Fe_3C/FeO_x@SNC/LNC, and Fe_3C/FeO_x@LNC.

observed. On the outside, NCNT consisted of 7−9 layers of graphene with interlamellar spacing of 0.34 nm. Inside it, the size of $Fe_3C/Co(Fe)O_x$ core was about 20 nm and it showed crystal lattice of around 0.21 nm, corresponding to the Fe_3C phase coating on the nanoparticle surface, which was obviously shown in Figure 1c. The elemental distribution of a typical $Fe_3C/Co(Fe)O_x$@NCNT was further studied using high-angle annular dark-field scanning transmission electron microscopy (HAADF-STEM) as shown in Figure 1d. Along the $Fe_3C/Co(Fe)O_x$@NCNT, it was obvious that carbon (red) and nitrogen (orange) distributed on the whole CNT, while oxygen (yellow), iron (green), and cobalt (blue) concentrate in the inside particle of the CNTs, further verifying formation of $Fe_3C/Co(Fe)O_x$@NCNT.

The surface chemical composition and element configuration elucidation of $Fe_3C/Co(Fe)O_x$@NCNT were further investigated with the aid of X-ray photoelectron spectroscopy (XPS) analysis. As shown in Table S1, there was an increasing nitrogen content—from 2.47 at. % at Fe_3C/FeO_x@LNC to 3.66 at. % at Fe_3C/FeO_x@SNC/LNC, then 6.98 at. % at $Fe_3C/Co(Fe)O_x$@NCNT—thereby suggesting the contribution of Co/Zn additive to improving nitrogen doping. There was also a decreasing trend in iron content from 3.41 at. % to 1.09 at. % and that may be attributed to the transformation from FeO_x to CoO_x. The long-range spectrum (Figure 2a) of $Fe_3C/Co(Fe)O_x$@NCNT clearly portrayed the presence of C (84.07 at. %), N (6.98 at. %), O (7.06 at. %), Fe (1.09 at. %), and Co (0.80 at. %) in the active material. The obviously strong peak located at 285.5 eV was the C 1s peak while the O 1s peak centered at 529.8 eV in $Fe_3C/Co(Fe)O_x$@NCNT confirmed the formation of metal oxide. Notably, the N content was extremely high, which not only pushed the Fermi level closer to conduction band making the carbon nanostructure more electronically conductive and disordered, but also can be more easily to form synergy between nitrogen and the transition metals, thus promoting catalytic activity.[42,43] The high-resolution N 1s spectrum was shown in Figure 2b and exhibited four existence forms of nitrogen including pyridinic-N at ∼398.7 eV, pyrrolic-N at ∼400 eV, graphitic-N at ∼401.2 eV, and Fe-N_x at ∼399.2 eV, in which the peak for graphitic-N was dominant. Although different nitrogen species possessed different chemical/electronic contexts for neighboring C so that to affect catalytic performance to various degrees, all of these nitrogen species were known for helping speed up the ORR process apart from oxidized-N, the specific role of which was not well understood. To study the intrinsic nature of chemical interaction between N and the transition metals, the Fe 2p spectrum and the Co 2p spectrum were further deconvoluted. Figure 2c presented the deconvoluted Fe 2p spectrum, where existed two sets of peaks for Fe^{2+} (710.6 and 722.3 eV) and Fe^{3+} (712.9 and 725.0 eV), confirming the existence of the chemical coupling between iron and N/C moieties.[42] Besides, there was also a satellite peak at ∼717.8 eV, suggesting the existence of FeO_x phase.[44] Similarly, the peaks in the Co 2p spectrum (Figure 2d) corresponded to both Co^{2+} and Co^{3+} forms, suggesting that Co species existed in the form of nitrides or oxides. Moreover, there was also a satellite peak at ∼785.80 eV corresponding to the oxide phase of Co.[42] All these characters were also confirmed by powder X-ray diffraction (XRD), as can be seen in Figure S2.

Raman spectrum was utilized to identify the situation of the different carbons. D band (1345 cm^{-1}) represented the defects in sp^3 hybridized carbon while G band (1592 cm^{-1}) represented in-plane vibration in graphitic sp^2 carbon structures, namely disorder and crystallinity, respectively.[14] The ratio of D band and G band intensities (I_D/I_G) decreased

DOI: 10.1021/acsami.7b02346
ACS Appl. Mater. Interfaces 2017, 9, 21216−21224

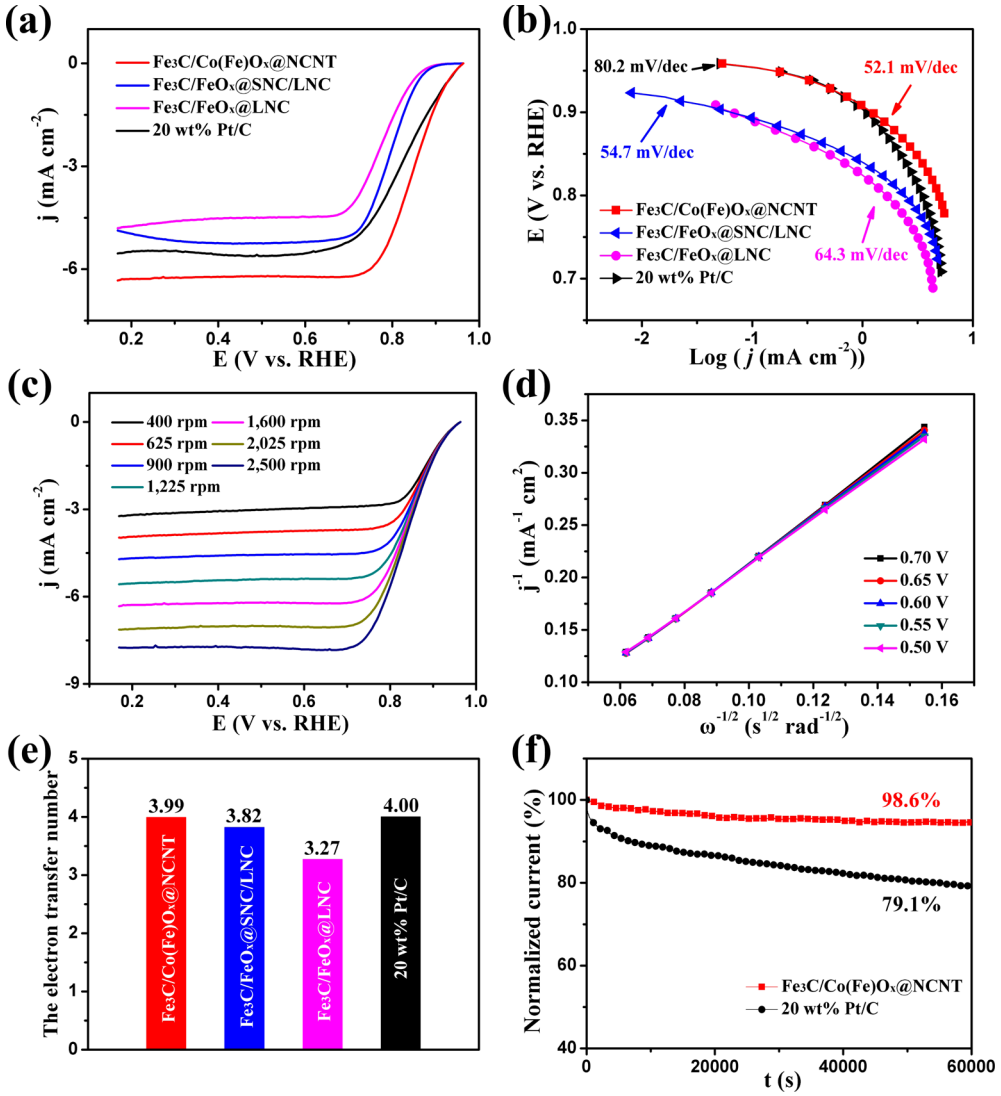

Figure 3. (a) ORR polarization curves and (b) Tafel plots of different samples in an O_2-saturated 0.1 M KOH at room temperature with a sweep rate of 10 mV s^{-1} at a rotation speed of 1600 rpm. (c) ORR polarization curves of $Fe_3C/Co(Fe)O_x$@NCNT at various rotating rates (scan rate = 10 mV s^{-1}). (d) Koutechy–Levich plots of $Fe_3C/Co(Fe)O_x$@NCNT at various potentials. (e) Comparison of the electron transfer number of the synthesized catalysts. (f) ORR current–time chronoamperometric response of $Fe_3C/Co(Fe)O_x$@NCNT and Pt/C in O_2-saturated 0.1 M KOH solution.

from 1.25 for Fe_3C/FeO_x@LNC to 1.15 for $Fe_3C/Co(Fe)O_x$@NCNT, which was beneficial to improve the electrical conductivity. The Brunauer–Emmett–Teller (BET) method was used to evaluate the specific surface area of $Fe_3C/Co(Fe)O_x$@NCNT, Fe_3C/FeO_x@SNC/LNC and Fe_3C/FeO_x@LNC, which were compared in Figure 2e. With the difference of Zn content in each precursors, these three materials exhibited the BET surface areas of 732.5, 878.9, and 372.7 m^2 g^{-1}, respectively. It was noteworthy that Fe_3C/FeO_x@SNC/LNC showed the largest specific surface area, arising from Zn's volatility character in nature, which can lead to higher level of porosity and nitrogen doping.[45,46]

With above desirable characterization, cyclic voltammetry (CV) method was first used to study the ORR catalytic performance of $Fe_3C/Co(Fe)O_x$@NCNT in O_2 versus N_2-satruated 0.1 M KOH solution. As shown in Figure S4, the CV of the $Fe_3C/Co(Fe)O_x$@NCNT obtained in N_2-satruated solution showed a featureless voltammetric current, while their corresponding CV obtained in the O_2-satruated solution exhibited a cathodic peak at ~0.81 V, which highly exceeded that of Fe_3C/FeO_x@SNC/LNC (0.77 V), Fe_3C/FeO_x@LNC (0.75 V), and Pt/C (0.76 V), suggesting the excellent ORR performance of the $Fe_3C/Co(Fe)O_x$@NCNT.

The ORR kinetics of $Fe_3C/Co(Fe)O_x$@NCNT was further studied by linear sweep voltammetry (LSV) method. A series of LSVs for different samples were collected by scanning the potentials at a sweeping rate of 10 mV s^{-1} at 1600 rpm. As can be seen in Figure 3a, Fe_3C/FeO_x@LNC exhibited undesirable ORR activity while Fe_3C/FeO_x@SNC/LNC, through the volatilization of Zn to achieve higher surface area with more nitrogen-doping, enhanced the electrocatalytic activity to a certain extent. $Fe_3C/Co(Fe)O_x$@NCNT obviously had the highest half-wave potential ($E_{1/2}$) of 0.86 V, significantly exceeding over that of Pt/C (0.83 V). This, together with its higher diffusion-limited current density compared with Pt/C, demonstrated comparatively higher mass transport of O_2 as a result of its exceptionally high electrochemically active surface area and strongly suggested that $Fe_3C/Co(Fe)O_x$@NCNT

DOI: 10.1021/acsami.7b02346
ACS Appl. Mater. Interfaces 2017, 9, 21216–21224

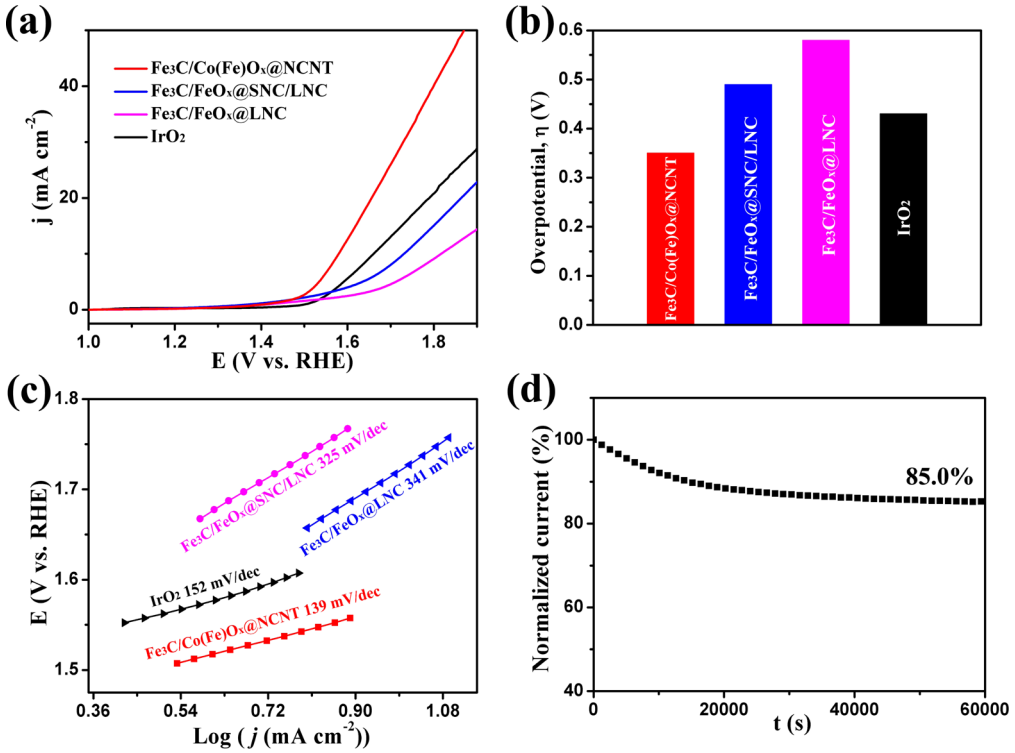

Figure 4. (a) OER polarization curves, (b) overpotentials for OER at 10 mA cm^{-2}, and (c) Tafel plots of $Fe_3C/Co(Fe)O_x$@NCNT, Fe_3C/FeO_x@SNC/LNC, Fe_3C/FeO_x@LNC, and IrO_2. (d) OER durability of $Fe_3C/Co(Fe)O_x$@NCNT.

were efficient ORR electrocatalysts. The superior ORR performance of $Fe_3C/Co(Fe)O_x$@NCNT was further verified by comparing the Tafel slopes of different samples. It turned out that Tafel slope for $Fe_3C/Co(Fe)O_x$@NCNT (52.1 mV per decade) was smaller than that of Pt/C (80.2 mV per decade), as well as other counterparts (Figure 3b). The much smaller Tafel slope corresponded to a more favorable ORR kinetics, reconfirming the high electrocatalytic activity toward ORR.

Another critical parameter for assessing ORR catalytic performance was the electron transfer number per O_2 molecule (n) so that more detailed LSV curves at different rotating rates were explored to quantitatively study the materials. With the increase of the rotation speed, the diffusion of O_2 at the surface of the electrode increased so that larger current densities can be obtained as shown in Figures 3c and S5. Through the Koutechy−Levich (K−L) equation, the link between the limiting diffusion current density (j) and the rotating speed (ω) can be calculated from LSVs and compared at different potentials. Figures 3d and S6 showed linear relationships of different samples between j^{-1} and $\omega^{-1/2}$ while the value of n can be calculated according to the K−L plots at various potentials. Obviously, when the potential ranged between 0.5 and 0.7 V, the values of n for $Fe_3C/Co(Fe)O_x$@NCNT were figured to be of 3.91−4.10, which approached Pt/C's theoretical value of 4.00 measured in the same environment, demonstrating an efficient 4e dominant process.[47] Moreover, other samples' electron transfer numbers were also calculated and compared at 0.55 V versus RHE in Figure 3e. Fe_3C/FeO_x@SNC/LNC also exhibited high electron transfer numbers while Fe_3C/FeO_x@LNC only possessed an n of 3.27, suggesting that oxygen reduction was dominated by two-electron process, which may be due to the incapacity of the oxygen absorption on Fe_3C/FeO_x@LNC.

In addition to catalytic performance, the ORR durability of $Fe_3C/Co(Fe)O_x$@NCNT and Pt/C were measured via chronoamperometric measurements in alkaline medium at a constant cathodic voltage of 0.5 V with a rotation speed of 1,600 rpm (Figure 3f). Over 60 000s of continuous operation, 94.5% of the original current density of $Fe_3C/Co(Fe)O_x$@NCNT can be retained due to the support of carbon framework as a highly conducting substrate and its desirable electrochemical combination with oxygen molecules. Under the same conditions, the Pt/C electrode showed 20.9% drop in current density, which may be caused by catalyst's regression after some period of time through surface oxidation, migration or aggregation of the Pt nanoparticles over long periods of operation.[29]

The electrocatalytic performances of different samples for OER were also investigated in O_2-saturated 0.1 M KOH solution. To explore the onset potential, LSVs of the catalysts were shown in Figure 4a at 1600 rpm. As can be seen in the LSVs, Fe_3C/FeO_x@SNC/LNC and Fe_3C/FeO_x@LNC exhibited relatively inferior OER responses while the anodic current of $Fe_3C/Co(Fe)O_x$@NCNT exhibited a lower onset potential at ∼1.50 V, which proved the critical role of the existence of cobalt−iron mixed metal oxides in enhancing OER activity. Moreover, the potential required to deliver the same current density of 10 mA cm^{-2} ($E_{j=10}$) were compared in Figure 4b, which was the desirable value to efficiently power solar water-splitting systems.[22] Along with the much lower onset potential, $Fe_3C/Co(Fe)O_x$@NCNT generated 10 mA cm^{-2} at 1.58 V, even 80 mV lower than that of IrO_2, and also more superior than other samples (1.72 V for Fe_3C/FeO_x@SNC/LNC, 1.81 V for Fe_3C/FeO_x@LNC). Through introducing cobalt and nitrogen dopants, their adjacent carbon atoms can be positively charged so that to benefit the adsorption of hydroxyl ions and accelerate the electron transportation among

DOI: 10.1021/acsami.7b02346
ACS Appl. Mater. Interfaces 2017, 9, 21216−21224

catalyst surfaces and reaction intermediates, thus facilitating oxygen reactions and improving OER activity. The superior OER performance was also compared with other reported materials and $Fe_3C/Co(Fe)O_x$@NCNT turned out to be one of the most efficient OER electrocatalysts (Table S2). The Tafel slope of $Fe_3C/Co(Fe)O_x$@NCNT was figured as 139 mV dec^{-1} (Figure 4c), which was much lower than that of Fe_3C/FeO_x@SNC/LNC (314 mV dec^{-1}), Fe_3C/FeO_x@LNC (325 mV dec^{-1}), and IrO_2 (152 mV dec^{-1}), demonstrating the desirable reaction kinetics during the OER process and further confirming the excellent electrochemical OER activity of $Fe_3C/Co(Fe)O_x$@NCNT. The OER stability of the catalyst was also assessed through the chronoamperometric measurement at a constant potential of 1.58 V and an excellent anodic current retention of 85% within 60 000 s was observed in the $Fe_3C/Co(Fe)O_x$@NCNT catalyst (Figure 4d), indicating its favorable stability in continuous OER process.

The overall oxygen electrode activity of $Fe_3C/Co(Fe)O_x$@NCNT was explored by hydrodynamic voltammetry in alkaline solution and compared with Fe_3C/FeO_x@SNC/LNC, Fe_3C/FeO_x@LNC, and Pt/C (Figure 5). The overvoltage between

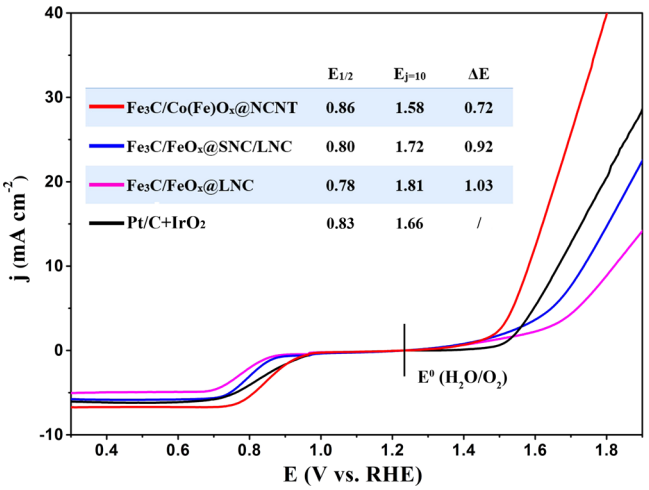

Figure 5. Overall LSV curves of $Fe_3C/Co(Fe)O_x$@NCNT, Fe_3C/FeO_x@SNC/LNC, Fe_3C/FeO_x@LNC, Pt/C, and IrO_2 catalysts in an O_2-saturated 0.1 M KOH at a rotation speed of 1,600 rpm (scan rate: 10 mV s^{-1}). Inset table shows comparison of bifunctional activity of $Fe_3C/Co(Fe)O_x$@NCNT, Fe_3C/FeO_x@SNC/LNC, Fe_3C/FeO_x@LNC, Pt/C, and IrO_2.

ORR and OER ($\Delta E = E_{j=10} - E_{1/2}$) represented efficiency loss during the whole process and was considered as a critical parameter for rating catalyst's bifunctional electrocatalytic activity. The smaller the ΔE value was, the closer the catalyst was to an ideal reversible oxygen electrode.[22] Dramatically, $Fe_3C/Co(Fe)O_x$@NCNT exhibited unprecedented overall oxygen electrode activity of 0.72 V, which was much more superior to that of Fe_3C/FeO_x@SNC/LNC (0.92 V) and Fe_3C/FeO_x@LNC (1.03 V). This oxygen electrode activity was compared with other previously reported (Table S2) catalysts and proved $Fe_3C/Co(Fe)O_x$/NCNT to be among the best bifunctional catalysts.

Considering the existence of the chemical coupling between iron and N/C moieties, there was one question about what roles they played in influencing the catalytic performance. Previous reports proposed two different mechanisms.[48,49] Therefore, further experiments were conducted to assess the role of iron in forming catalytic active sites. Cyanide ions (CN^-) was known to be able to forcefully coordinate with iron so that iron-based catalytic sites would be poisoned while nitrogen active sites were inert to CN^-.[50] Thus, ORR activity of $Fe_3C/Co(Fe)O_x$@NCNT was tested in 0.1 M KOH with the presence of 10 mM KCN to verify whether iron-containing species were the actual active sites for catalyzing oxygen reaction and if so, its activity would decrease to a certain extent after cyanide treatment. The LSV curves of $Fe_3C/Co(Fe)O_x$@NCNT in Figure S7 showed 50 mV and 120 mV diminishment in onset and half-wave potential, respectively, after the addition of KCN, indicating the contribution of iron−nitrogen coordination sites in catalytic activity. As for OER activity, there was no doubt that cobalt-based metal oxides played the critical role in enhancing OER activity according to the greatly improved OER performance from Fe_3C/FeO_x@SNC/LNC to $Fe_3C/Co(Fe)O_x$@NCNT. In conclusion, these results clearly showed that the coordination between iron and N/C moieties ensured superior activity toward ORR while cobalt-based metal oxides were responsible for excellent OER activity. Thus, $Fe_3C/Co(Fe)O_x$@NCNT possessed remarkable electrocatalytic performance and excellent electrochemical durability for oxygen reactions, making it a highly promising candidate as a superior bifunctional oxygen electrocatalyst for practical application.

To evaluate the practical utility of $Fe_3C/Co(Fe)O_x$@NCNT in Zn−air batteries, we tested it in primary Zn-air battery first. The air cathode was prepared by uniformly coating $Fe_3C/Co(Fe)O_x$@NCNT on the carbon fiber paper and a polished Zn plate was used as the anode electrode. The polarization curves of $Fe_3C/Co(Fe)O_x$@NCNT and Pt/C were shown in Figure 6a and the power density plots were obtained according to the curve. When using 6 M KOH as the electrolyte, Zn-air batteries using $Fe_3C/Co(Fe)O_x$@NCNT as cathode material delivered an open circuit voltage of 1.48 V, a high current density of 177.5 mA cm^{-2} at 1.0 V and the maximum power density of 231 mW cm^{-2}, respectively, which were significantly exceeding over those of Pt/C. Moreover, no obvious potential drop was observed after galvanostatic discharging for 30 h at 5 mA cm^{-2} and 18 h at 10 mA cm^{-2} (Figure 6b), demonstrating favorable ORR stability. The durability of $Fe_3C/Co(Fe)O_x$@NCNT was also explored in rechargeable batteries and meanwhile, adding 0.2 M $Zn(CH_3COO)_2$ into the electrolyte to maintain reversible zinc electrochemical reactions at the anode.[51] In order to be a desirable bifunctional catalyst, high discharging voltage, low charging voltage, and minimal gap between two voltages were required for rechargeable battery.[52,53] Figure 6c showed the charging and discharging polarization curves for Zn-air battery and the much low charge−discharge voltage gap of 0.88 V at 50 mA cm^{-2} was observed, indicating a better rechargeability. Moreover, when maintaining current rate at 10 mA cm^{-2} during the cycling (Figure 6d), the final charge and discharge potential of $Fe_3C/Co(Fe)O_x$/NCNT were observed at ∼2.06 and ∼1.14 V with an overall voltage gap of 0.92 V after 150 cycles (about 25 h), exhibiting no obvious drop compared with the initial values of ∼2.03 and ∼1.15 V, respectively. In contrast, although Pt/C cathode delivered a slight lower charge voltage during the first cycle, its performance was noticeably deteriorated after the fifth cycle, reconfirming the excellent durability of $Fe_3C/Co(Fe)O_x$/NCNT. Besides the virtually negligible voltage fading, all above-mentioned results shown by $Fe_3C/Co(Fe)O_x$@NCNT electrode demonstrated its great potential to be applied in zinc-air

DOI: 10.1021/acsami.7b02346
ACS Appl. Mater. Interfaces 2017, 9, 21216−21224

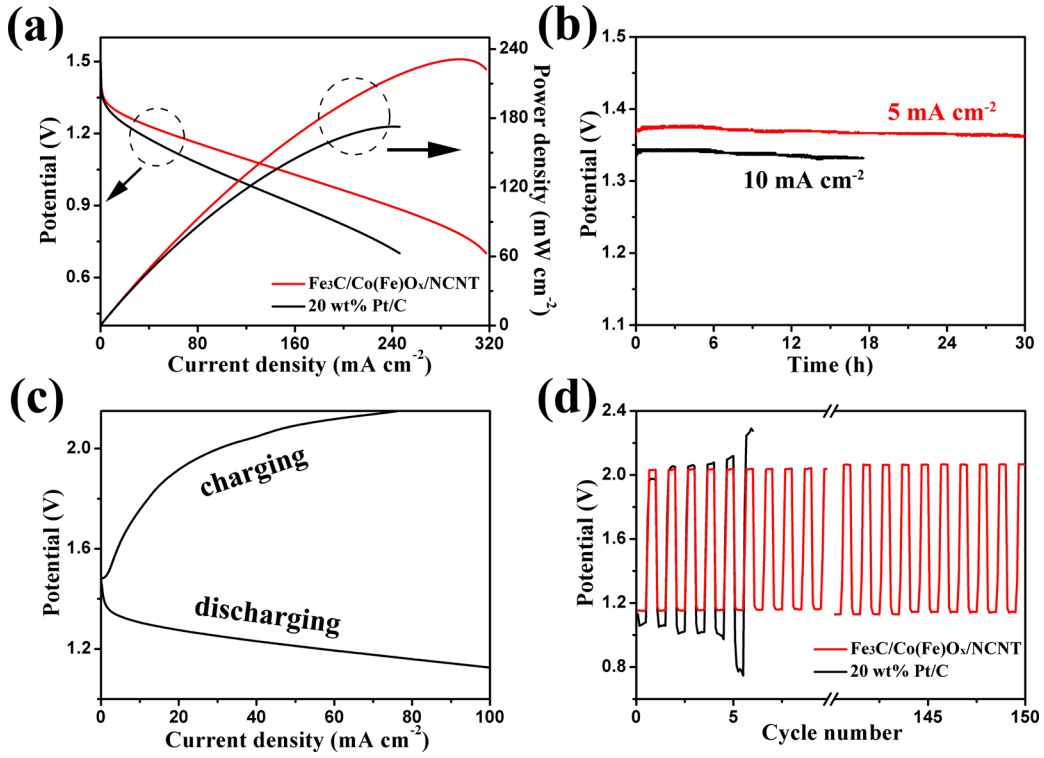

Figure 6. (a) Discharge voltage curve (v−i) and the corresponding power density plot using the Pt/C and $Fe_3C/Co(Fe)O_x$@NCNT air electrode. (b) Discharge curves of the primary Zn−air batteries using $Fe_3C/Co(Fe)O_x$@NCNT as ORR catalyst and KOH electrolyte at various current densities (5 and 10 mA cm^{-2}). (c) Charge and discharge polarization curves. (d) Discharge/charge cycling curves of two-electrode rechargeable Zn−air batteries using the Pt/C and $Fe_3C/Co(Fe)O_x$@NCNT air electrode at a current density of 10 mA cm^{-2}.

battery, which can be attributed to the catalyst's superior OER and ORR performance in alkaline solution.

CONCLUSION

In summary, we integrated the merits of nitrogen-doped carbon materials and metal oxide to synthesize $Fe_3C/Co(Fe)O_x$@NCNT using PPy-Fe coordination complex as precursors with Co−Zn additive, for the first time, affording $Fe_3C/Co(Fe)O_x$ nanoparticles encapsuled into several sections of NCNT. During the carbonization process, PPy-Fe coordination complex not only provided carbon and nitrogen source for development of NCNTs but also served as iron source for the formation of Fe−N_x moieties to improve ORR activity, while Zn^{2+} of Co−Zn gradually volatilized to enhance the specific surface area and Co element was oxidized to further facilitate oxygen reaction. The as-prepared $Fe_3C/Co(Fe)O_x$@NCNT exhibited remarkable electrocatalytic activity, not only outperforming common noble metal-based catalyst, but also showing much better performances than most of reported bifunctional electrocatalysts. The synthesis strategy reported here can be used for the development of many other NCNT-supported bifunctional materials and allowed new avenues for synthesizing highly active NCNT-supported ORR and OER electrocatalysts, which would be highly promising candidates for developing new generation of renewable energy systems.

ASSOCIATED CONTENT

Supporting Information

The Supporting Information is available free of charge on the ACS Publications website at DOI: 10.1021/acsami.7b02346.

Experimental section, TEM images, elemental composition, XRD pattern, Raman spectrum, CV curves, LSV curves at different rotation speeds, K−L plots of different materials, LSV curves without and in the presence of cyanide ions, electrocatalytic properties for different samples (PDF)

AUTHOR INFORMATION

Corresponding Authors

*E-mail: tqian@suda.edu.cn.
*E-mail: c.yan@suda.edu.cn.

ORCID

Tao Qian: 0000-0001-7252-8224
Chenglin Yan: 0000-0003-4467-9441

Notes

The authors declare no competing financial interest.

ACKNOWLEDGMENTS

This work was supported by the National Natural Science Foundation of China (Nos. 51402202 and 51622208).

REFERENCES

(1) Eberle, U.; von Helmolt, R. Sustainable Transportation Based on Electric Vehicle Concepts: A Brief Overview. *Energy Environ. Sci.* **2010**, *3*, 689−699.

(2) Sengodan, S.; Choi, S.; Jun, A.; Shin, T. H.; Ju, Y.-W.; Jeong, H. Y.; Shin, J.; Irvine, J. T. S.; Kim, G. Layered Oxygen-Deficient Double Perovskite as an Efficient and Stable Anode for Direct Hydrocarbon Solid Oxide Fuel Cells. *Nat. Mater.* **2015**, *14*, 205−209.

(3) Wang, Y.-J.; Zhao, N.; Fang, B.; Li, H.; Bi, X. T.; Wang, H. Carbon-Supported Pt-Based Alloy Electrocatalysts for the Oxygen Reduction Reaction in Polymer Electrolyte Membrane Fuel Cells:

DOI: 10.1021/acsami.7b02346
ACS Appl. Mater. Interfaces 2017, 9, 21216−21224

Particle Size, Shape, and Composition Manipulation and Their Impact to Activity. *Chem. Rev.* **2015**, *115*, 3433−3467.
(4) Lee, J.-S.; Kim, S. T.; Cao, R.; Choi, N.-S.; Liu, M.; Lee, K. T.; Cho, J. Metal-Air Batteries with High Energy Density: Li-Air versus Zn-Air. *Adv. Energy Mater.* **2011**, *1*, 34−50.
(5) Cheon, J. Y.; Kim, K.; Sa, Y. J.; Sahgong, S. H.; Hong, Y.; Woo, J.; Yim, S.-D.; Jeong, H. Y.; Kim, Y.; Joo, S. H. Graphitic Nanoshell/Mesoporous Carbon Nanohybrids as Highly Efficient and Stable Bifunctional Oxygen Electrocatalysts for Rechargeable Aqueous Na-Air Batteries. *Adv. Energy Mater.* **2016**, *6*, 1501794.
(6) Jin, Y.; Wang, H.; Li, J.; Yue, X.; Han, Y.; Shen, P. K.; Cui, Y. Porous MoO_2 Nanosheets as Non-Noble Bifunctional Electrocatalysts for Overall Water Splitting. *Adv. Mater.* **2016**, *28*, 3785−3790.
(7) Wang, H.; Lee, H.-W.; Deng, Y.; Lu, Z.; Hsu, P.-C.; Liu, Y.; Lin, D.; Cui, Y. Bifunctional Non-Noble Metal Oxide Nanoparticle Electrocatalysts through Lithium-Induced Conversion for Overall Water Splitting. *Nat. Commun.* **2015**, *6*, 7261−7268.
(8) Stern, L.-A.; Feng, L.; Song, F.; Hu, X. Ni_2P as a Janus Catalyst for Water Splitting: The Oxygen Evolution Activity of Ni_2P Nanoparticles. *Energy Environ. Sci.* **2015**, *8*, 2347−2351.
(9) Wu, G.; More, K. L.; Johnston, C. M.; Zelenay, P. High-Performance Electrocatalysts for Oxygen Reduction Derived from Polyaniline, Iron, and Cobalt. *Science* **2011**, *332*, 443−447.
(10) Li, D.; Wang, C.; Strmcnik, D. S.; Tripkovic, D. V.; Sun, X.; Kang, Y.; Chi, M.; Snyder, J. D.; van der Vliet, D.; Tsai, Y.; Stamenkovic, V. R.; Sun, S.; Markovic, N. M. Functional Links between Pt Single Crystal Morphology and Nanoparticles with Different Size and Shape: The Oxygen Reduction Reaction Case. *Energy Environ. Sci.* **2014**, *7*, 4061−4069.
(11) Huang, X.; Zhao, Z.; Cao, L.; Chen, Y.; Zhu, E.; Lin, Z.; Li, M.; Yan, A.; Zettl, A.; Wang, Y. M.; Duan, X.; Mueller, T.; Huang, Y. High-Performance Transition Metal−Doped Pt_3Ni Octahedra for Oxygen Reduction Reaction. *Science* **2015**, *348*, 1230−1234.
(12) Petrykin, V.; Macounova, K.; Shlyakhtin, O. A.; Krtil, P. Tailoring the Selectivity for Electrocatalytic Oxygen Evolution on Ruthenium Oxides by Zinc Substitution. *Angew. Chem., Int. Ed.* **2010**, *49*, 4813−4815.
(13) Sanchez Casalongue, H. G.; Ng, M. L.; Kaya, S.; Friebel, D.; Ogasawara, H.; Nilsson, A. In Situ Observation of Surface Species on Iridium Oxide Nanoparticles during the Oxygen Evolution Reaction. *Angew. Chem., Int. Ed.* **2014**, *53*, 7169−7172.
(14) Yang, W.; Liu, X.; Yue, X.; Jia, J.; Guo, S. Bamboo-like Carbon Nanotube/Fe_3C Nanoparticle Hybrids and Their Highly Efficient Catalysis for Oxygen Reduction. *J. Am. Chem. Soc.* **2015**, *137*, 1436−1439.
(15) Lu, X.; Yim, W.-L.; Suryanto, B. H. R.; Zhao, C. Electrocatalytic Oxygen Evolution at Surface-Oxidized Multiwall Carbon Nanotubes. *J. Am. Chem. Soc.* **2015**, *137*, 2901−2907.
(16) Liu, T.; Guo, Y.-F.; Yan, Y.-M.; Wang, F.; Deng, C.; Rooney, D.; Sun, K.-N. CoO Nanoparticles Embedded in Three-Dimensional Nitrogen/Sulfur Co-Doped Carbon Nanofiber Networks as a Bifunctional Catalyst for Oxygen Reduction/Evolution Reactions. *Carbon* **2016**, *106*, 84−92.
(17) Li, B.; Geng, D.; Lee, X. S.; Ge, X.; Chai, J.; Wang, Z.; Zhang, J.; Liu, Z.; Hor, T. S. A.; Zong, Y. Eggplant-Derived Microporous Carbon Sheets: Towards Mass Production of Efficient Bifunctional Oxygen Electrocatalysts at Low Cost for Rechargeable Zn-air Batteries. *Chem. Commun.* **2015**, *51*, 8841−8844.
(18) Yang, Z.; Yao, Z.; Li, G.; Fang, G.; Nie, H.; Liu, Z.; Zhou, X.; Chen, X.; Huang, S. Sulfur-Doped Graphene as an Efficient Metal-free Cathode Catalyst for Oxygen Reduction. *ACS Nano* **2012**, *6*, 205−211.
(19) Liang, Y.; Li, Y.; Wang, H.; Zhou, J.; Wang, J.; Regier, T.; Dai, H. Co_3O_4 Nanocrystals on Graphene as a Synergistic Catalyst for Oxygen Reduction Reaction. *Nat. Mater.* **2011**, *10*, 780−786.
(20) Geng, D.; Ding, N.; Hor, T. S. A.; Liu, Z.; Sun, X.; Zong, Y. Potential of Metal-Free "Graphene Alloy" as Electrocatalysts for Oxygen Reduction Reaction. *J. Mater. Chem. A* **2015**, *3*, 1795−1810.
(21) Kannari, N.; Itakura, T.; Ozaki, J. Electrochemical Oxygen Reduction Activity of Intermediate Onion-like Carbon Produced by the Thermal Transformation of Nanodiamond. *Carbon* **2015**, *87*, 415−417.
(22) Qu, K.; Zheng, Y.; Dai, S.; Qiao, S. Z. Graphene Oxide-Polydopamine Derived N, S-Codoped Carbon Nanosheets as Superior Bifunctional Electrocatalysts for Oxygen Reduction and Evolution. *Nano Energy* **2016**, *19*, 373−381.
(23) Jin, J.; Pan, F.; Jiang, L.; Fu, X.; Liang, A.; Wei, Z.; Zhang, J.; Sun, G. Catalyst-Free Synthesis of Crumpled Boron and Nitrogen Co-Doped Graphite Layers with Tunable Bond Structure for Oxygen Reduction Reaction. *ACS Nano* **2014**, *8*, 3313−3321.
(24) Fei, H.; Ye, R.; Ye, G.; Gong, Y.; Peng, Z.; Fan, X.; Samuel, E. L. G.; Ajayan, P. M.; Tour, J. M. Boron- and Nitrogen-Doped Graphene Quantum Dots/Graphene Hybrid Nanoplatelets as Efficient Electrocatalysts for Oxygen Reduction. *ACS Nano* **2014**, *8*, 10837−10843.
(25) Vineesh, T. V.; Kumar, M. P.; Takahashi, C.; Kalita, G.; Alwarappan, S.; Pattanayak, D. K.; Narayanan, T. N. Bifunctional Electrocatalytic Activity of Boron-Doped Graphene Derived from Boron Carbide. *Adv. Energy Mater.* **2015**, *5*, 1500658.
(26) Pels, J. R.; Kapteijn, F.; Moulijn, J. A.; Zhu, Q.; Thomas, K. M. Evolution of Nitrogen Functionalities in Carbonaceous Materials During Pyrolysis. *Carbon* **1995**, *33*, 1641−1653.
(27) Zhang, J.; Xia, Z.; Dai, L. Carbon-Based Electrocatalysts for Advanced Energy Conversion and Storage. *Sci. Adv.* **2015**, *1*, e1500564.
(28) Duan, J.; Chen, S.; Jaroniec, M.; Qiao, S. Z. Heteroatom-Doped Graphene-Based Materials for Energy-Relevant Electrocatalytic Processes. *ACS Catal.* **2015**, *5*, 5207−5234.
(29) Gong, K.; Du, F.; Xia, Z.; Durstock, M.; Dai, L. Nitrogen-Doped Carbon Nanotube Arrays with High Electrocatalytic Activity for Oxygen Reduction. *Science* **2009**, *323*, 760−765.
(30) Dai, L.; Xue, Y.; Qu, L.; Choi, H.-J.; Baek, J.-B. Metal-Free Catalysts for Oxygen Reduction Reaction. *Chem. Rev.* **2015**, *115*, 4823−4892.
(31) Xia, B. Y.; Yan, Y.; Li, N.; Wu, H. B.; Lou, X. W.; Wang, X. A Metal-Organic Framework-Derived Bifunctional Oxygen Electrocatalyst. *Nat. Energy* **2016**, *1*, 15006−15013.
(32) Aijaz, A.; Masa, J.; Rosler, C.; Xia, W.; Weide, P.; Botz, A. J. R.; Fischer, R. A.; Schuhmann, W.; Muhler, M. Co@Co_3O_4 Encapsulated in Carbon Nanotube-Grafted Nitrogen-Doped Carbon Polyhedra as an Advanced Bifunctional Oxygen Electrode. *Angew. Chem., Int. Ed.* **2016**, *55*, 4087−4093.
(33) Li, B.; Chen, Y.; Ge, X.; Chai, J.; Zhang, X.; Hor, T. S. A.; Du, G.; Liu, Z.; Zhang, H.; Zong, Y. Mussel-Inspired One-Pot Synthesis of Transition Metal and Nitrogen Co-Doped Carbon (M/N-C) as Efficient Oxygen Catalysts for Zn-Air Batteries. *Nanoscale* **2016**, *8*, 5067−5075.
(34) Liu, Z.-Q.; Cheng, H.; Li, N.; Ma, T. Y.; Su, Y.-Z. $ZnCo_2O_4$ Quantum Dots Anchored on Nitrogen-Doped Carbon Nanotubes as Reversible Oxygen Reduction/Evolution Electrocatalysts. *Adv. Mater.* **2016**, *28*, 3777−3784.
(35) Li, Q.; Pan, H.; Higgins, D.; Cao, R.; Zhang, G.; Lv, H.; Wu, K.; Cho, J.; Wu, G. Metal−Organic Framework-Derived Bamboo-like Nitrogen-Doped Graphene Tubes as an Active Matrix for Hybrid Oxygen-Reduction Electrocatalysts. *Small* **2015**, *11*, 1443−1452.
(36) Tung, C.-W.; Hsu, Y.-Y.; Shen, Y.-P.; Zheng, Y.; Chan, T.-S.; Sheu, H.-S.; Cheng, Y.-C.; Chen, H. M. Reversible Adapting Layer Produces Robust Single-Crystal Electrocatalyst for Oxygen Rvolution. *Nat. Commun.* **2015**, *6*, 8106−8114.
(37) Zhan, Y.; Xu, C.; Lu, M.; Liu, Z.; Lee, J. Y. Mn and Co Co-Substituted Fe_3O_4 Nanoparticles on Nitrogen-Doped Reduced Graphene Oxide for Oxygen Electrocatalysis in Alkaline Solution. *J. Mater. Chem. A* **2014**, *2*, 16217−16223.
(38) Liu, X.; Park, M.; Kim, M. G.; Gupta, S.; Wang, X.; Wu, G.; Cho, J. High-Performance Non-Spinel Cobalt−Manganese Mixed Oxide-Based Bifunctional Electrocatalysts for Rechargeable Zinc−Air Batteries. *Nano Energy* **2016**, *20*, 315−325.
(39) Kargar, A.; Yavuz, S.; Kim, T. K.; Liu, C.-H.; Kuru, C.; Rustomji, C. S.; Jin, S.; Bandaru, P. R. Solution-Processed $CoFe_2O_4$ Nano-

DOI: 10.1021/acsami.7b02346
ACS Appl. Mater. Interfaces 2017, 9, 21216−21224

particles on 3D Carbon Fiber Papers for Durable Oxygen Evolution Reaction. *ACS Appl. Mater. Interfaces* **2015**, *7*, 17851−17856.
(40) Qian, T.; Wu, S.; Shen, J. Facilely Prepared Polypyrrole-Reduced Graphite Oxide Core-Shell Microspheres with High Dispersibility for Electrochemical Detection of Dopamine. *Chem. Commun.* **2013**, *49*, 4610−4612.
(41) Zhou, J.; Qian, T.; Yang, T.; Wang, M.; Guo, J.; Yan, C. Nanomeshes of Highly Crystalline Nitrogen-Doped Carbon Encapsulated Fe/Fe_3C Electrodes as Ultrafast and Stable Anodes for Li-Ion Batteries. *J. Mater. Chem. A* **2015**, *3*, 15008−15014.
(42) Palaniselvam, T.; Kashyap, V.; Bhange, S. N.; Baek, J.-B.; Kurungot, S. Nanoporous Graphene Enriched with Fe/Co-N Active Sites as a Promising Oxygen Reduction Electrocatalyst for Anion Exchange Membrane Fuel Cells. *Adv. Funct. Mater.* **2016**, *26*, 2150−2162.
(43) Wu, G.; Santandreu, A.; Kellogg, W.; Gupta, S.; Ogoke, O.; Zhang, H.; Wang, H.-L.; Dai, L. Carbon Nanocomposite Catalysts for Oxygen Reduction and Evolution Reactions: From Nitrogen Doping to Transition-Metal Addition. *Nano Energy* **2016**, *29*, 83−110.
(44) Niu, W.; Li, L.; Liu, X.; Wang, N.; Liu, J.; Zhou, W.; Tang, Z.; Chen, S. Mesoporous N-Doped Carbons Prepared with Thermally Removable Nanoparticle Templates: An Efficient Electrocatalyst for Oxygen Reduction Reaction. *J. Am. Chem. Soc.* **2015**, *137*, 5555−5562.
(45) Chen, Y.-Z.; Wang, C.; Wu, Z.-Y.; Xiong, Y.; Xu, Q.; Yu, S.-H.; Jiang, H.-L. From Bimetallic Metal-Organic Framework to Porous Carbon: High Surface Area and Multicomponent Active Dopants for Excellent Electrocatalysis. *Adv. Mater.* **2015**, *27*, 5010−5016.
(46) Gadipelli, S.; Zhao, T.; Shevlin, S. A.; Guo, Z. Switching Effective Oxygen Reduction and Evolution Performance by Controlled Graphitization of a Cobalt-Nitrogen-Carbon Framework System. *Energy Environ. Sci.* **2016**, *9*, 1661−1667.
(47) Ge, X.; Sumboja, A.; Wuu, D.; An, T.; Li, B.; Goh, F. W. T.; Hor, T. S. A.; Zong, Y.; Liu, Z. Oxygen Reduction in Alkaline Media: From Mechanisms to Recent Advances of Catalysts. *ACS Catal.* **2015**, *5*, 4643−4667.
(48) Li, J.; Ghoshal, S.; Liang, W.; Sougrati, M.-T.; Jaouen, F.; Halevi, B.; McKinney, S.; McCool, G.; Ma, C.; Yuan, X.; Ma, Z.-F.; Mukerjee, S.; Jia, Q. Structural and Mechanistic Basis for the High Activity of Fe-N-C Catalysts toward Oxygen Reduction. *Energy Environ. Sci.* **2016**, *9*, 2418−2432.
(49) Jeong, B.; Shin, D.; Choun, M.; Maurya, S.; Baik, J.; Mun, B. S.; Moon, S.-H.; Su, D.; Lee, J. Nitrogen-Deficient ORR Active Sites Formation by Iron-Assisted Water Vapor Activation of Electrospun Carbon Nanofibers. *J. Phys. Chem. C* **2016**, *120*, 7705−7714.
(50) Ferrero, G. A.; Preuss, K.; Marinovic, A.; Jorge, A. B.; Mansor, N.; Brett, D. J. L.; Fuertes, A. B.; Sevilla, M.; Titirici, M.-M. Fe-N-Doped Carbon Capsules with Outstanding Electrochemical Performance and Stability for the Oxygen Reduction Reaction in Both Acid and Alkaline Conditions. *ACS Nano* **2016**, *10*, 5922−5932.
(51) Li, Y.; Dai, H. Recent Advances in Zinc−Air Batteries. *Chem. Soc. Rev.* **2014**, *43*, 5257−5275.
(52) Chen, Z.; Yu, A.; Higgins, D.; Li, H.; Wang, H.; Chen, Z. W. Highly Active and Durable Core−Corona Structured Bifunctional Catalyst for Rechargeable Metal−Air Battery Application. *Nano Lett.* **2012**, *12*, 1946−1952.
(53) Wang, M.; Qian, T.; Zhou, J.; Yan, C. An Efficient Bifunctional Electrocatalyst for a Zinc-Air Battery Derived from Fe/N/C and Bimetallic Metal-Organic Framework Composites. *ACS Appl. Mater. Interfaces* **2017**, *9*, 5213−5221.

DOI: 10.1021/acsami.7b02346
ACS Appl. Mater. Interfaces 2017, 9, 21216−21224